X-ray Absorption Spectroscopy and Magnetism of Synthetic Greigite and Greigite Magnetosomes in Magnetotactic Bacteria

Xiaohui Zhu, Adam P. Hitchcock, Lucas Le Nagard, Dennis A. Bazylinski, Viviana Morillo, Fernanda Abreu, Pedro Leão & Ulysses Lins

Taylor & Francis
Taylor & Francis Group

Check for updates

X-ray Absorption Spectroscopy and Magnetism of Synthetic Greigite and Greigite Magnetosomes in Magnetotactic Bacteria

Xiaohui Zhu[a], Adam P. Hitchcock[a], Lucas Le Nagard[a], Dennis A. Bazylinski[b], Viviana Morillo[b], Fernanda Abreu[c], Pedro Leão[c], and Ulysses Lins[c]

[a]Department of Chemistry and Chemical Biology, McMaster University, Hamilton, ON, Canada; [b]School of Life Sciences, University of Nevada at Las Vegas, Las Vegas, NV, USA; [c]Departamento de Microbiologia Geral, Universidade Federal do Rio de Janeiro, Rio de Janeiro, RJ, Brazil

ABSTRACT

Scanning transmission X-ray microscopy at the Fe 2p ($L_{2,3}$), O1s, C1s, and S2p edges was used to study greigite magnetosomes and other cellular content of a magnetotactic bacterium known as a multicellular magnetotactic prokaryote (MMP). X-ray absorption spectrum (XAS) and X-ray magnetic circular dichroism (XMCD) spectra of greigite (Fe_3S_4) nanoparticles, synthesized via a hydrothermal method, were measured. Although XAS of the synthetic greigite nanoparticles and biotic magnetosome crystals in MMPs are slightly different due to partial oxidation of the MMP greigite, the XMCD spectra of the two materials are in good agreement. The Fe 2p XAS and XMCD spectra of Fe_3S_4 are quite different from those of its oxygen analog, magnetite (Fe_3O_4), suggesting Fe_3S_4 has a different electronic and magnetic structure than Fe_3O_4 despite having the same crystal structure. Sulfate and sulfide species were also identified in MMPs, both of which are likely involved in sulfur metabolism.

Introduction

Magnetotactic bacteria (MTB) are a diverse group of gram-negative, motile and mostly aquatic prokaryotes, which employ the Earth's geomagnetic field to navigate toward favorable habitats (Bazylinski and Frankel 2004; Faivre and Schüler 2008). This behavior is a result of the presence of intracellular magnetic particles known as magnetosomes which consist of membrane-bounded crystals of the magnetic minerals magnetite (Fe_3O_4) or greigite (Fe_3S_4) (Bazylinski and Frankel 2004). Magnetosomes are typically organized as chains within the cell. The net magnetic moment of such chains is sufficient to align the cell with the Earth's geomagnetic field lines (Frankel 1984). Most known single-celled MTB biomineralize Fe_3O_4 magnetosomes (Frankel 1984), while only multicellular magnetotactic prokaryotes (MMPs) and several single-celled, rod-shaped bacteria produce Fe_3S_4 magnetosomes (Bazylinski et al. 1993; Farina et al. 1990; Heywood et al. 1990; Lefèvre et al. 2011; Rodgers et al. 1990). Although one strain of both Fe_3O_4 and Fe_3S_4-producing MTB has been isolated and grown in axenic culture (Lefèvre et al. 2011), most remain resistant to culturing. Therefore, much less is known about Fe_3S_4-producing MTB compared to their magnetite-producing counterparts.

MMPs are one of the most interesting MTB due to their unique multicellular morphology (Farina et al. 1980). They have been detected in a large number of aquatic, mostly marine, habitats (Bazylinski et al. 1990; Delong et al. 1993; Farina et al. 1980; Keim et al. 2006; Simmons et al. 2004). Most MMPs are

roughly spherical, cell aggregates with a diameter varying between 3 and 12 μm (Keim et al. 2006). Typically they are composed of approximately 10–40 genetically identical gram-negative cells that are tightly bound to one another and radially organized around an internal acellular compartment located at the center of the whole organism (Farina et al. 1980; Keim et al. 2006, 2004). Transmission electron microscopy (TEM) of ultra-thin sections of MMPs further shows that the internal compartment is surrounded by filament fibers that link each cell together (Keim et al. 2006, 2004). Membrane vesicles are also present in the internal compartment and are thought to be involved in cell-to-cell communication (Keim et al. 2006, 2004). Recently, another kind of MMP with an ellipsoidal, rather than spherical morphology was described (Zhou et al. 2012). It is composed of ∼40 cells but arranged in interlaced circles. In most cases, MMPs biomineralize Fe_3S_4 magnetosome chains, but some MMPs synthesize only bullet-shaped Fe_3O_4 crystals or both bullet-shaped Fe_3O_4 and Fe_3S_4 crystals, even in the same chain (Lins et al. 2007; Zhang et al. 2014).

MMPs represent an important model for understanding cell evolution, multicellularity, and biomineralization in bacteria (Keim et al. 2006). The dominant mineral phase in magnetosomes produced by MMPs is greigite (Fe_3S_4) although two non-magnetic iron-sulfur minerals have also been observed. These are mackinawite (tetragonal FeS) and a cubic form of FeS (Pósfai et al. 1998a, 1998b), which are thought to be precursors to Fe_3S_4. Greigite and the pyrrhotites ($Fe_{1-x}S$, $0 < x < 0.13$) are the two

major ferromagnetic iron-sulfide minerals (Letard et al. 2005). Because Fe_3S_4 was thought to be thermodynamically metastable under sedimentary conditions, its geological importance in sediments was previously underestimated (Berner 1984; Roberts 1995; Roberts et al. 1996). However over the last few decades, there has been increasing evidence that greigite can persist in the geological record of sediments for long periods of time (Porreca et al. 2009; Porreca and Mattei 2010; Roberts et al. 2011; Snowball and Thompson 1988). Thus, if greigite magnetosomes can be preserved as magnetofossils in environments such as soils, rocks, and sediments, they may be a significant paleomagnetic carrier that may provide information regarding the history, properties, and behavior of the geomagnetic field (Roberts 1995; Roberts et al. 2011).

Greigite is a thiospinel of iron (Pearce et al. 2006, Rickard and Luther 2007). Similar to magnetite, its oxygen analog, Fe_3S_4 is a mixed valence compound with Fe(II) and Fe(III) occupying the octahedral and tetrahedral sites. However, the site distribution of Fe(II) and Fe(III) in Fe_3S_4 is not well understood (Chang et al. 2012a; Letard et al. 2005). The magnetic properties of Fe_3S_4 have been characterized using several techniques including Mössbauer spectroscopy (Lin et al. 2014), ferromagnetic resonance spectroscopy (Chang et al. 2012b), neutron scattering (Chang et al. 2009), and superconducting quantum interference device magnetometry (Feng et al. 2013).

Recently, synchrotron-based scanning transmission X-ray microscopy (STXM) has attracted attention as a technique for biomineralization studies due to its capability to image, identify, and quantitate electronic and chemical structures of elements at a spatial resolution down to ∼30 nm via near edge X-ray absorption fine structure spectroscopy (Hitchcock 2015). Compared with non-spatially resolved spectroscopies and other spectromicroscopies, STXM has many advantages including good spatial resolution, high sensitivity to chemical structures, high energy (spectral) resolution, and relatively small radiation damage. Together, these factors make STXM a suitable tool to study biogeochemical and environmental samples (Hitchcock et al. 2012; Lawrence et al. 2012; Rema et al. 2014) as well as radiation-sensitive nanostructures (Zhu et al. 2015a).

X-ray magnetic circular dichroism (XMCD) is a synchrotron-based technique, which provides quantitative information about elemental and site-specific magnetism in magnetic materials (Stöhr and Siegmann 2006). The XMCD signal is defined as the difference of the two X-ray absorption spectra (XAS) recorded with circularly polarized X-rays when the photon spin and magnetic moment in the sample are aligned parallel and antiparallel. XMCD measured with STXM (STXM-XMCD) has been successfully applied to probe chemistry and biomagnetism in the unicellular MTB, *Magnetovibrio blakemorei* strain MV-1, at the single cell and even single magnetosome level (Kalirai et al. 2013, 2012; Lam et al. 2010; Zhu et al. 2016, 2015b). It has also been used to examine extracellular magnetic iron minerals biomineralized by *Shewanella oneidensis* strain MR-1 (Coker et al. 2012).

Several groups have reported non-spatially resolved Fe 2p XAS and XMCD spectra of greigite (Bauer et al. 2014; Chang et al. 2012a; Letard et al. 2005; Pattrick et al. 2017). Some literature spectra show only a single peak in the L_3 region while others exhibit a two-peak feature with an additional peak at higher energy. The higher energy feature was attributed to the surface oxidization of the sample (Chang et al. 2012a; Pattrick et al. 2017). In this study, we use STXM at the Fe $L_{2,3}$ edge to compare the XAS and XMCD spectra of synthetic greigite, and greigite magnetosomes in an MMP, with the aim of better understanding the magnetic structure of greigite, as well as Fe_3S_4 magnetosome biomineralization in these interesting microorganisms. The paper is organized as follows. After describing sample preparation and experimental methods, the XAS and XMCD spectra of synthesized greigite are presented and discussed. The Fe 2p, S2p, O1s, and C1s spectromicroscopy of an MMP are then presented. XMCD magnetic studies of the biogenic greigite magnetosomes in an MMP are described, and the results compared to those for synthetic greigite.

Materials and methods

Preparation and TEM characterization of MMPs

Environmental MMP samples were used in this study. Water and sediment were collected at Araruama Lagoon (22°52'49.3"S, 42°07'04.5"W) in Rio de Janeiro, Brazil. An additional sample was collected from the Salton Sea (33°30'11.2"N, 115°54'51.7"W) in California, USA. MMPs were magnetically isolated with a customized glass flask and home-made coil, as previously described (Lins et al. 2003). A droplet of magnetically enriched MMPs was deposited on Formvar-coated TEM copper grids. After several washes with distilled water, the grid was dried in air and then anaerobically transported to the synchrotron facility for STXM measurements. The high-resolution transmission electron microscopy (HRTEM) and energy-dispersive X-ray spectrometer (EDS) analysis of magnetosomes in MMPs were carried out using a FEI FEG G20 TEM device operated at 200 kV using scanning transmission electron microscope (STEM) mode. Fast Fourier transforms (FFTs) of high-resolution calibrated lattice images were obtained using Digital Micrograph software (Gatan Inc.).

Synthesis and characterization of Fe_3S_4 nanoparticles

Abiotic Fe_3S_4 nanoparticles were prepared by the hydrothermal reaction of ferric chloride ($FeCl_3 \cdot 6H_2O$) with thiourea [$SC(NH_2)_2$] in aqueous ethylene glycol ($C_2H_6O_2$) solution at 180 °C for 12 h, as described by Zhang and Chen 2009.The phase composition of the as-synthesized Fe_3S_4 sample was determined by powder X-ray diffraction (XRD) using a Bruker D8 Advance instrument with Co Kα radiation. The elemental composition of the sample was measured with the EDS on a JEOL 7000 F scanning electron microscope (SEM), and found to be stoichiometric. For STXM-XMCD analysis, the Fe_3S_4 nanoparticles were sonically dispersed in ethanol and a droplet of the solution was deposited onto a Formvar-coated copper grid. The grid sample was anaerobically transported to the synchrotron facility for analysis.

STXM-XMCD measurements

Measurements were carried out using the ambient STXM device at beamline 10ID-1at the Canadian Light Source (CLS)

and the STXM device at beamline 11.0.2 at the Advanced Light Source (ALS). Both of these beamlines use an elliptically polarizing undulator (EPU) as the radiation source. The CLS 10ID-1 line operates in first harmonic and provides nearly 100% circularly polarized light at the Fe $L_{2,3}$ region. Due to a lower ring energy, the ALS 11.0.2 EPU is operated in third harmonic at the Fe $L_{2,3}$ edge which provides highly elliptical radiation with 90% circularly polarized light. Details about these two beamlines have been reported elsewhere (Kaznatcheev et al. 2007; Warwick et al. 2004) while the STXM instrumentation, which is very similar for the ALS and CLS undulator beamlines, has been described by Kilcoyne et al. (2003). Since the magnetosome chains in the MMP sample are located in the plane of the TEM grid, and the strength of the XMCD signal is proportional to the projection of sample magnetization along the propagation direction of X-ray beam, the sample was mounted at a 30° angle about the long axis of the sample plate such that 50% of the in-plane magnetization vector of horizontally oriented magnetosomes is projected onto the X-ray beam direction. A 0.5-T magnet was used to magnetize the Fe_3S_4 nanoparticles before XMCD measurement (Roberts et al. 2011) was made. However, an external magnetic field was not applied in the case of MMPs since the goal of the study is to probe the unperturbed internal magnetic moment. Both samples were measured in a magnetic field-free environment.

In STXM, monochromatic X-rays with a specific polarization illuminate a Fresnel zone plate (diameter of 240 μm, outer zone width of 25 nm, 95 μm central stop, obtained from the Centre for X-ray Optics, Lawrence Berkeley National Lab), which focuses the X-rays to a ~30-nm spot on the sample. Images are generated by raster-scanning the sample while measuring the transmitted X-rays using a phosphor to convert X-rays to visible light, followed by single event counting using a photomultiplier tube detector (Kilcoyne et al. 2003). A sequence of images or "stack" (Jacobsen et al. 2000), which covers the energy region of interest, is recorded for spectroscopic analysis. It takes several hours to record a full (~140 point) Fe $L_{2,3}$ XMCD spectrum, over which time the system response can change. In order to reduce the influence of those time-dependent drifts on the final result a concurrent acquisition mode is used, which alternates the circular polarization of X-rays between parallel and antiparallel to the magnetization of the sample at each energy point. Previously we have shown that spectral data collected with this concurrent mode are less dependent on beamline stability and carbon build-up than the previously used successive mode in which parallel and antiparallel stacks are recorded sequentially (Kalirai et al. 2012; Lam et al. 2010).

Data analysis was performed using aXis2000 (Hitchcock 2016). For the STXM-XMCD analysis, the parallel and antiparallel stacks were appended and aligned together. I (x,y, E), the transmitted signal at each pixel (x,y) at each energy (E), is converted to optical density [OD $= -\ln(I/I_o)$], where I_o is measured from an area adjacent to the region of interest but free of the mineral or MMP sample. After image alignment and conversion to optical density, each pixel in the image stack contains an XAS spectrum. The XMCD spectrum is obtained from the difference of two XAS spectra extracted from the same spatial region, but recorded with opposite circular polarization.

Results and discussion

### S $L_{2,3}$ and Fe $L_{2,3}$ spectroscopy of synthetic Fe_3S_4 nanoparticles

The powder XRD pattern of the hydrothermally produced Fe_3S_4 nanoparticles is presented in Figure 1. Two mineral phases were identified—one was Fe_3S_4 (diffraction peaks identified by red circles) and the other was mackinawite (tetragonal FeS) (blue rhombus). According to semi-quantitative analysis, Fe_3S_4 was identified as the major phase. The minority mackinawite phase was estimated to be ~10 wt%. The presence of mackinawite in the sample may be due to decomposition of Fe_3S_4 which occurs at ~190 °C under hydrothermal conditions (Uda 1965). Mackinawite is non-magnetic at ambient temperature, so that its presence should not have a detectable effect on the XMCD spectrum, aside from reducing the XMCD intensity relative to that of a pure greigite sample.

The S 2p X-ray absorption spectrum of hydrothermal Fe_3S_4 nanoparticles is shown in Figure 2, panel A. Supplemental Figure S1A (see supplemental information) shows a STXM image of the Fe_3S_4 nanoparticles at 710 eV. Supplemental Figure S1B presents the appended S2p, O1s, and Fe2p XAS of the same cluster of Fe_3S_4 nanoparticles. The O 1s XAS signal is very weak, consistent with the near-stoichiometric composition as measured by EDS in an SEM. In the EDS analysis the atomic ratio of S to Fe was 1.14, which is lower than the value of 1.33 (4/3) expected for stoichiometric Fe_3S_4, consistent with the synthesized Fe_3S_4 nanoparticles being slightly oxidized, as is observed by XAS. It is worth noting that the EDS analysis was performed 10 days after the STXM measurement. During this period, the sample was exposed to air so the atomic ratio of S to Fe might be underestimated if the S was partially replaced with O atoms during air oxidization.

The S 2p spectrum of the Fe_3S_4 nanoparticles exhibits four features which are labeled A, B, C, and D in Figure 2A. The S 2p spectrum of greigite is similar to S 2p spectra reported for other thiospinels such as linnaeite (Co_3S_4) and carrollite ($CuCo_2S_4$) (Li et al. 1995). According to Li et al. (1995), peak A
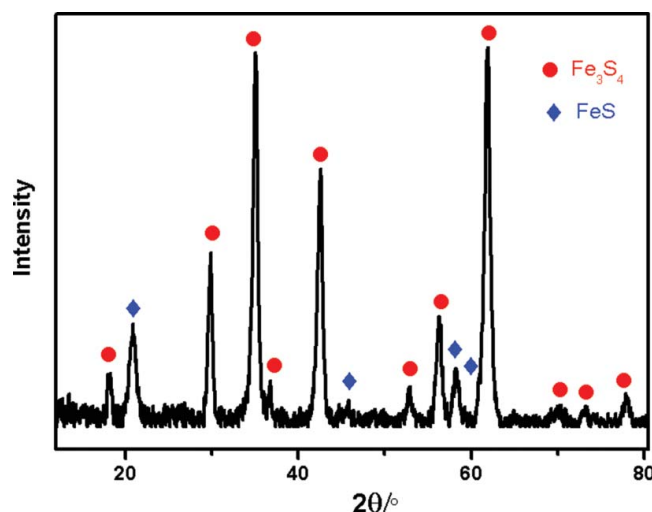
Figure 1. X-ray powder diffraction (XRD) pattern of the chemically produced Fe_3S_4 nanoparticles, recorded using Co K_α radiation. Two mineral phases are identified: one is greigite (Fe_3S_4) (peaks labeled with red circles); the other is mackinawite (FeS) (peaks labeled with blue rhombi).
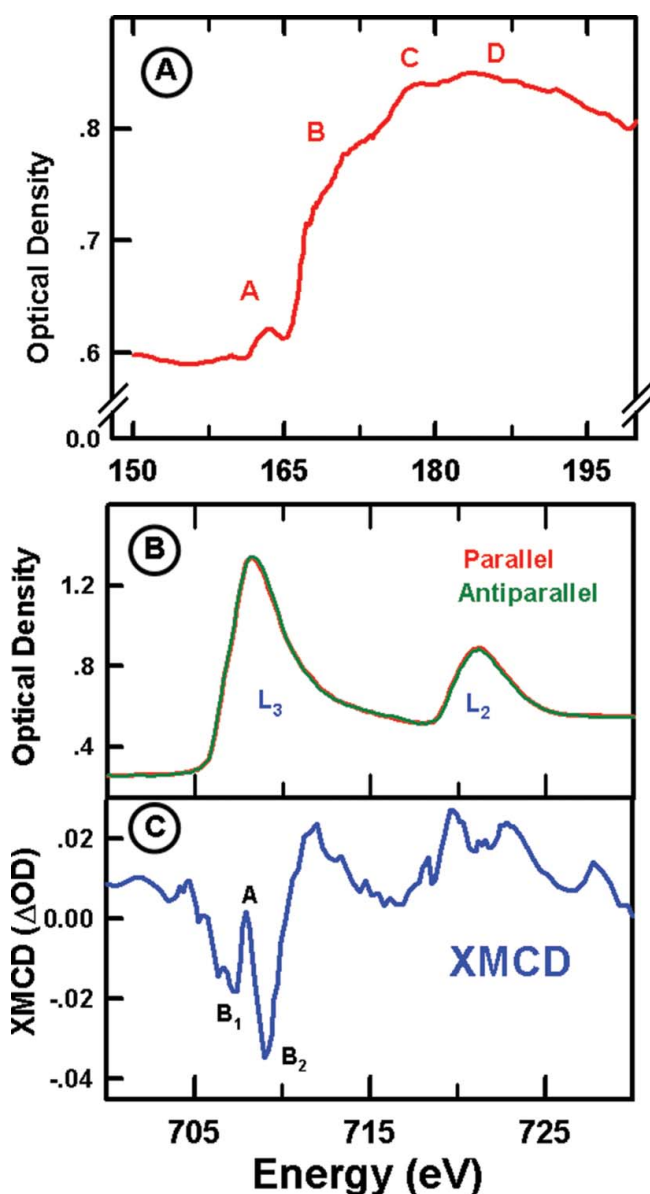
Figure 2. (A) S 2p X-ray absorption spectrum (XAS) of hydrothermally synthesized Fe_3S_4 nanoparticles. An image of the greigite cluster, and a composite S-O-Fe spectrum is presented in supplemental Figure S-1. (B) Fe $L_{2,3}$-edge XAS of the same Fe_3S_4 nanoparticles recorded with circularly polarized X-rays parallel (red) and antiparallel (green) to the magnetization of the sample. (C) Fe L_{23} X-ray magnetic circular dichroism (XMCD, blue) taken as the difference of the parallel spectrum minus the antiparallel spectrum.

et al. (2012a), which showed a two-peak feature with an energy separation of 1.5 eV in the L_3 energy region instead of the single, asymmetric peak presented in Figure 2B. Chang et al. (2012a) claimed that the high-energy peak in their XAS was due to the presence of a non-magnetic, oxidized layer on the Fe_3S_4 crystal surface, which dominated the Fe $L_{2,3}$ XAS signal since the surface-sensitive total-electron-yield (TEY) detection mode was used to acquire the XAS in their study. Letard et al. (2005) also observed an amorphous shell surrounding Fe_3S_4 grains using electron energy loss spectroscopy (EELS) in a TEM analysis. The shape of the EELS spectra of Fe_3S_4 they reported is similar to that of Chang et al. (2012a), but has a different energy scale. Recently, Bauer et al. (2014) reported the Fe $L_{2,3}$ XAS of Fe_3S_4 crystals which showed only a single peak in the L_3 region, similar to that presented in Figure 2B. By comparing the Fe 2p XAS of greigite and pure, elemental Fe, Bauer et al. (2014) claimed that their greigite sample contained a large amount of Fe. However, despite having a similar spectrum, the XRD analysis (Figure 1) clearly excludes the presence of any elemental iron in our sample.

Figure 2C plots the XMCD spectrum of Fe_3S_4 nanoparticles, obtained by taking the difference between the two XAS shown in Figure 2B. It agrees with the XMCD spectrum of nanoparticle greigite reported by Pattrick et al. (2017). The XMCD spectrum of greigite exhibits three characteristic peaks in the L_3 region located at 707.1 (feature B_1), 708.0 (A), and 709.1 eV (B_2). Since Fe_3S_4 is structurally a ferrimagnetic inverse spinel (Pattrick et al. 2002; Rickard and Luther 2007), similar to Fe_3O_4, these three peaks are thought to correspond to three different iron sites in the Fe_3S_4 crystal structure: d^6 O_h (octahedral Fe^{2+} site, peak B_1), d^5T_d (tetrahedral Fe^{3+} site, peak A), and d^5O_h (octahedral Fe^{3+} site, peak B_2). However the three peaks in the Fe L_3 XMCD spectrum of Fe_3O_4 occur at 708.1, 709.1, and 709.9 eV (Goering et al. 2007; Zhu et al. 2015b). It is possible that the differences in bond lengths and effective charges between Fe_3O_4 and Fe_3S_4 crystals are responsible for the shift to lower energy of the XMCD and XAS spectral features (Chang et al. 2012a). In addition to the energy shift, the shape of the Fe_3S_4 XMCD spectrum is quite different from that of Fe_3O_4. Letard et al. (2005) claimed the difference in the XMCD spectra was due to the presence of iron vacancies in Fe_3S_4. Chang et al. (2012a) reported a similar XMCD spectrum of Fe_3S_4 as reported by Letard et al. (2005) but they found the same Fe_3S_4 sample had almost full Fe occupancy with neutron diffraction (Chang et al. 2009).

Identification of greigite magnetosomes in MMPs by TEM

Figure 3, panel A, presents a STEM image of an MMP collected from the Salton Sea, which shows that magnetosomes are scattered throughout the whole MMP organism. Figure 3B–D are TEM images corresponding to the regions labeled with red, blue, and green in Figure 3A, respectively. As shown in Figure 3B–D, the magnetosomes in MMP have two different morphologies: one is an irregular rectangular type indicated by red arrows and the other is an elongated-prismatic morphology indicated by blue arrows. Wang et al. (2013) reported that magnetosomes of some rod-shaped bacteria with different morphologies are made of different mineral phases. For example,

corresponds to transitions of S 2p electrons to S 3s-like states mixed with unoccupied Fe 3d crystal-field bands in the band gap; shoulder B is due to transitions to S 3s-like states; and peaks C and D are attributed to transitions of S 2p electron to t_{2g} and e_g S 3d states.
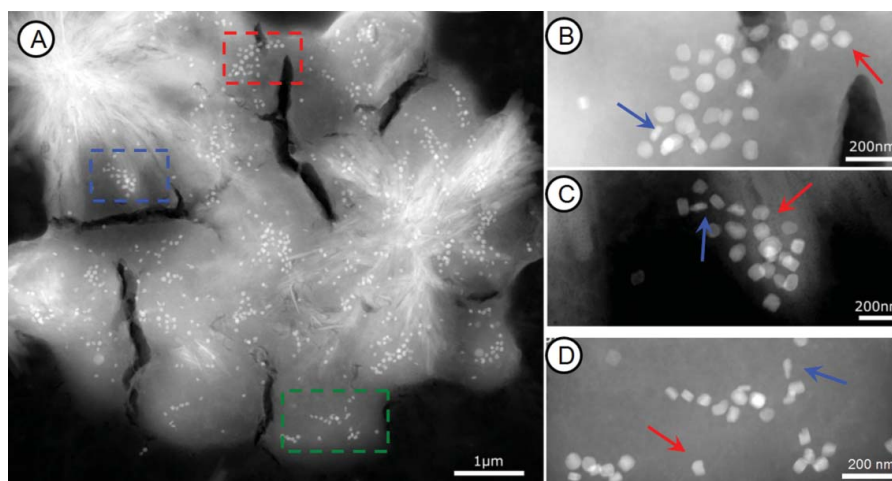
Fe $L_{2,3}$ X-ray absorption spectra of the Fe_3S_4 nanoparticles recorded with circularly polarized X-rays parallel and antiparallel to the sample magnetization are shown in Figure 2B. Note that the spectra measured with the two different circularly polarized X-rays are so close to one another that they cannot be distinguished in the plot. Two main peaks are present in the Fe $L_{2,3}$ XAS which are due to the spin-orbit splitting of the Fe 2p core level into the L_3 ($2p_{3/2}$) and L_2 ($2p_{1/2}$) components. Our XAS is very different from that of Fe_3S_4 reported by Chang

Figure 3. (A) Scanning transmission electron microscopy (STEM) image of MMPs found in the Salton Sea. (B~D) are STEM images corresponding to the red, blue, and green rectangle regions in Figure 3A, respectively. The red and blue arrows indicate magnetosomes with pleomorphic and elongated-prismatic morphology, respectively.

they found that a magnetosome with irregular rectangular morphology was composed of greigite while that with bullet-shaped morphology was made of magnetite (Wang et al. 2013). Therefore, HRTEM images of these two types of magnetosomes were measured in order to determine their mineral phases. Figure 4, panel A, presents a HRTEM image of the magnetosome with irregular rectangular morphology. Figure $4A_1$ shows the FFT image of the boxed region in Figure 4A and A_2 is the high-magnification image of the boxed region. The FFT in Figure $4A_1$ is along the zone axis (ZA) $[-1, 1, 2]$; the diffraction maxima of the FFT pattern were indexed to those of greigite. Figure 4B shows a HRTEM image of the magnetosome with elongated-prismatic morphology. Figure $4B_1$ and B_2 shows the FFT and high-magnification image of the boxed region in Figure 4B, respectively. The FFT pattern in Figure $4B_1$ is along the ZA $[2, -3, 3]$. As in the case of the irregular rectangular magnetosomes, the diffraction maxima in the FFT image of elongated-prismatic magnetosomes were identified as those of greigite. These TEM results indicate that, despite having different morphologies, the magnetosomes in the Salton Sea MMPs are composed exclusively of greigite. Energy dispersive X-ray spectroscopy on these TEM samples (see supplemental Figure S2) also confirms the presence of Fe and S in stoichiometric abundances.

Elemental distributions in MMPs measured by STXM

Figure S3 shows transmission STXM images of several MMPs from the Araruama Lagoon sample, recorded at the Fe L_3 edge (708.3 eV). Of the 4 MMPs shown in Figure S3, the MMP in Figure S3C was selected for detailed chemical study and that in Figure S3D for magnetic study. A method called "stack map" was used to characterize the distributions of sulfidic sulfur, and elemental carbon, oxygen, and iron in the whole MMP cell in Figure S3C. A stack map is the difference between two STXM OD images, one recorded at a characteristic X-ray absorption energy (on-resonance) and the other at a pre-edge energy (off-resonance). Figure 5, panels A-D show stack maps of $S_{sulfide}$, C, O, and Fe within an MMP, derived from the difference of pairs of STXM OD images at 190.5/168.2, 285.2/278,

540/528, and 708.3/700 eV, respectively. The STXM OD images at these eight energies are presented in Figure S4. The numbers on the upper and lower right side of each image (Figure S4) and the stack maps (Figure 5A–D) refer to the OD limits of the
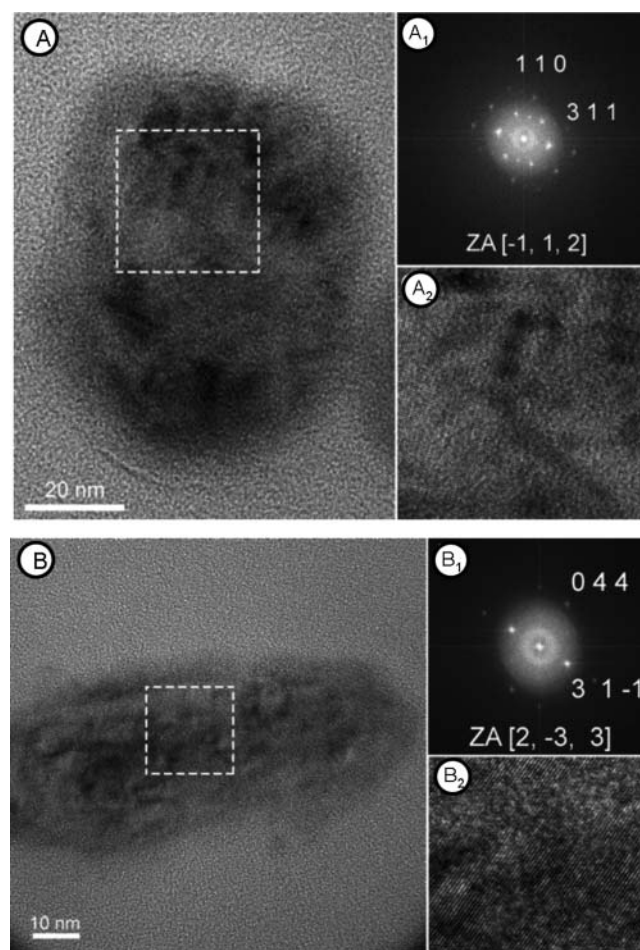
Figure 4. (A) High-resolution TEM (HRTEM) image of the magnetosome with pleomorphic morphology; A_1 shows the Fast Fourier Transform (FFT) of the boxed region in Figure 4A and A_2 is the high-magnification image of the boxed region. Note that the FFT pattern in figure $4A_1$ is along zone axis (ZA) $[-1, 1, 2]$; (B) HRTEM image of the magnetosome with elongated-prismatic morphology; B_1 and B_2 are FFTs of the high-magnification image of the boxed region in figure 4B. The FFT pattern in figure $4B_1$ is aligned along zone axis $[2, -3, 3]$ (Salton Sea).
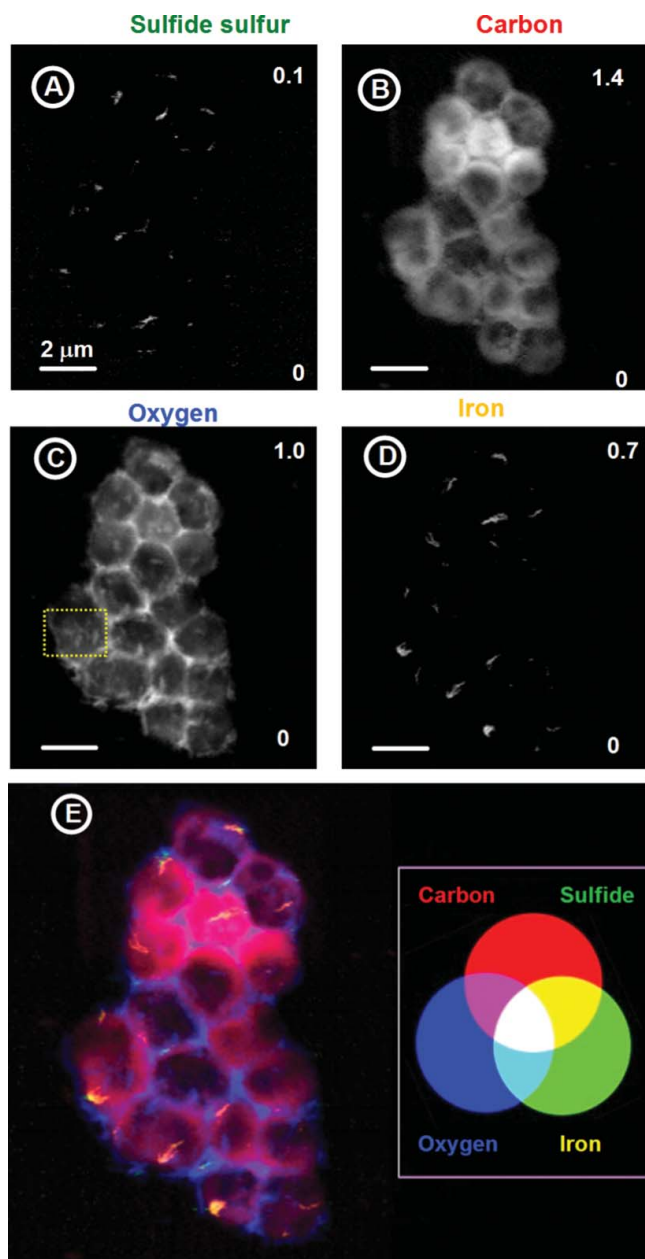
Figure 5. Maps of (A) sulfidic S, and (B) elemental C, (C) elemental O, and (D) elemental Fe in a multicellular magnetotactic prokaryote (MMP). The pre-edge and on-resonance images used to generate these maps are displayed in supplemental Figure S-4. (E) A re-scaled color composite of the $S_{sulfide}$ (green), C (red), O (blue), and Fe (yellow) maps (Araruama Lagoon).

gray scale display. Figure 5E is a re-scaled color composite of the sulfidic sulfur (green), carbon (red), oxygen (blue), and Fe (yellow) stack maps to show the spatial correlation of these elements. In most unicellular MTB cells, magnetosomes are arranged in chains that lie along the long axis of the cell such that the magnetic moment of the chain is maximized, which provides preferred orientation of the cells in an aquatic environment (Frankel 1984). However, magnetosomes inside MMPs (yellow in Figure 5E) are not arranged as long chains but as aggregates or clumps and short chains at multiple locations at the periphery of the cells (Keim et al. 2004). Thus, the magnetic moment in an MMP is not maximized in the same way as is typically found in unicellular MTB.

There is a strong O signal distributed widely throughout the MMP as shown in Figure 5C, which is associated with the organic material of the cell (e.g., protein, lipids etc.), and oxygen in phosphates and sulfates. The large intensity at the internal boundaries of the cells is due to sulfate from the aqueous environment, as identified in the detailed S 2p analysis. Some oxygen-rich regions (inside the yellow rectangle in Figure 5C) are also present surrounding Fe_3S_4 magnetosome clusters. When compared to the carbon, oxygen, and iron signals, the S 2p signal is much weaker within MMPs. A detailed presentation and analysis of the S 2p spectromicroscopy is given below.

Since MMPs inhabit marine environments where there are substantial amounts of chlorides and sulfates, sulfate and chloride are found in and around MMPs, even at the same location as the intracellular Fe_3S_4 magnetosomes. In order to extract the S 2p signal from the magnetosomes the Fe 2p stack was appended and aligned with the S 2p stack in order to use the Fe L_3 signal to identify the location of the magnetosomes and then use that information to extract the S 2p spectrum exclusively from the magnetosomes. Figure 6, panel A, shows the S 2p spectra of sulfate, chloride, and magnetosomes. In each case these spectra were isolated from mixed species signal by subtracting the clearly identified Cl 2p signal from the sulfate and the magnetosome spectra, and the sulfate spectrum from the chloride and magnetosome spectra. The spectrum of sulfate has two sharp features (A and B) which are assigned to transition of S 2p electrons to S 3s-like state and to S 3d-like states, respectively (Hay et al. 2004; Li et al. 1995). The sharp features in the 200~213-eV energy range (C) are attributed to Cl 2p → Cl 3d transitions. Figure 6B presents the spectra in the Fe 2p region of the chloride-rich, sulfate-rich, and magnetosome regions, which are the same regions from which the S 2p spectra in Figure 6A were extracted. These Fe 2p spectra were subjected to the same manipulation to isolate spectra of the pure components. There is a weak Fe 2p signal in the sulfate regions, but negligible Fe 2p signal in the chloride regions.

Singular value decomposition (SVD) (Koprinarov et al. 2002) was used to derive component maps for each species from the combined and aligned stack which includes the S 2p, Cl 2p, and Fe 2p spectral regions. The spectra in Figure 6 were used as reference spectra for the fit. The component maps of magnetosomes, chloride, and sulfate derived by the SVD fit are presented in Figure 7, panels A, B, and C, respectively. Figure 7D is a re-scaled color composite of the sulfate (red), chloride (green), and magnetosome (blue) maps. There is a significant amount of chloride all over the MMP organism, while the sulfate is predominantly in the intercellular region.

Magnetic measurements on MMPs

Figure 8, panels A and B, shows STXM OD images of the MMP (Figure S2d) recorded at 707 eV with left and right-circularly polarized X-rays, respectively. Note 707 eV is where the first XMCD peak of Fe_3S_4 magnetosomes occurs. The red dotted rectangle in Figure 8A indicates the region where the spectroscopic studies are performed. Acosta-Avalos et al. (2012) proposed a magnetic configuration model for MMP. By assuming that the cellular magnetic moment is given by the vector sum of the magnetic moments of the magnetosomes in each
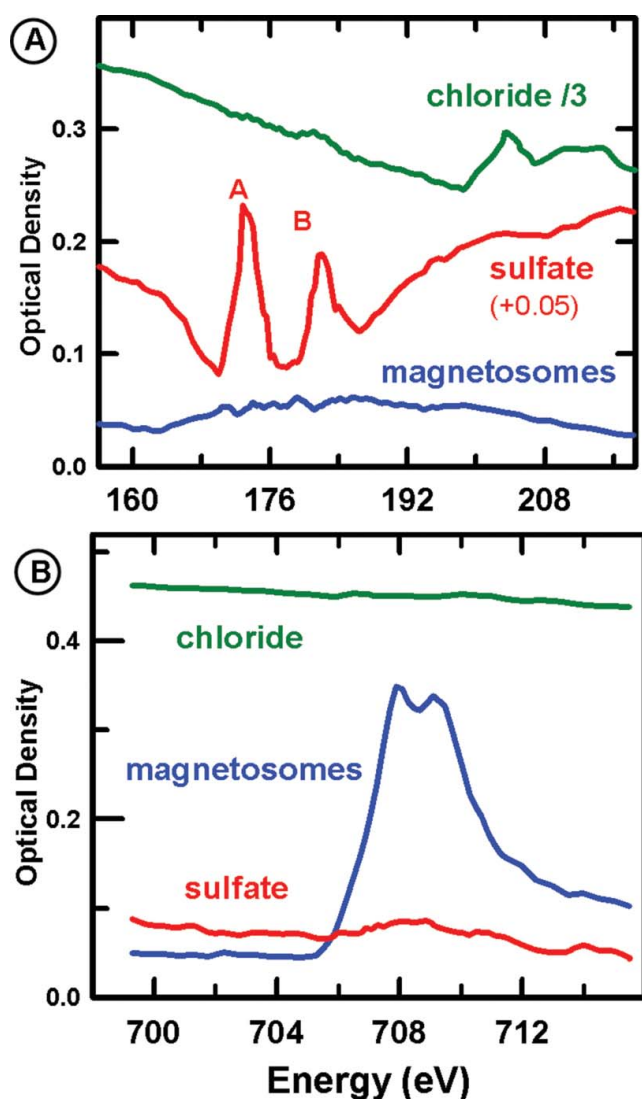
Figure 6. (A) S 2p XAS of sulfate (red), chloride (green), and magnetosomes (blue). The spectra are on a common optical density scale, with scaling for the chloride and a small offset for the sulfate, for clarity. The chloride and sulfate spectra were obtained by removing the contributions of the other species from spectra extracted from areas with majority signal. The spectrum of the magnetosomes was obtained by pixels identified from the Fe L_3 signal. A strong chloride signal and a small amount of sulfate signal were subtracted to get the clean S 2p spectrum of the magnetosomes. (B) Fe 2p XAS of the three components sulfate (red), chloride (green), and magnetosomes (blue), after the processing to get clean S 2p of the sulfate and magnetosomes and a clean Cl 2p spectrum of the chloride (Salton Sea).

pyrrhotite (Fe_7S_8) and found that this feature decreased when the sample surface was removed, although the XMCD signals did not change with the elimination of the sample surface. Thus, Letard et al. (2007) attributed this high-energy feature to an oxide layer surrounding the Fe_7S_8 surface and concluded that this surface oxide was not magnetic and thus did not contribute to the XMCD signal. Figure 9B compares the Fe $L_{2,3}$ XMCD spectra of Fe_3S_4 nanoparticles and Fe_3S_4 magnetosomes. The XMCD spectra of these two materials are rather similar, even though the XAS is different, suggesting that the difference between the XAS of abiotic (Figure 2A) and biotic Fe_3S_4 (Figure 9A) might be caused by surface oxidization of the biotic Fe_3S_4 magnetosomes. A previous study also showed the presence of an oxygen-rich amorphous phase at the surface but absent from the core of magnetosomes in MMPs (Lins and Farina 2001).

In order to probe the mechanism and kinetics of oxidation of biotic Fe_3S_4 magnetosomes in MMPs, we tracked the spectral changes of the Fe_3S_4 as MMPs were exposed to air over time. Figure 10 shows the Fe L_3 XAS of Fe_3S_4 magnetosomes in MMPs when exposed to air for less than one week (fresh), after three months, after one year, and after four years. Clearly, the intensity of peak B relative to peak A increases with the time of air exposure. This supports the interpretation of the additional feature observed at ~709.5 eV in biotic Fe_3S_4 magnetosomes (Figure 9), but not in abiotic Fe_3S_4 nanoparticles (Figure 2B), as being associated with partial oxidization. Another prominent spectral change occurred when MMPs were exposed to air for over four years—the higher energy peak now dominates the Fe L_3 spectrum. After this length of time the surface-oxidized layer on Fe_3S_4 was converted to hematite (α-Fe_2O_3), whose L_3 XAS is very close to that obtained from Fe_3S_4 magnetosomes exposed to air for over four years (Zhu et al. 2015b). Thus, it seems likely that Fe_3S_4 magnetosomes in MMPs stored under air slowly convert to hematite.

Discussion

Several groups have reported Fe 2p XAS and XMCD spectra of greigite (Bauer et al. 2014; Chang et al. 2012a; Letard et al. 2005; Pattrick et al. 2017). One of our challenges and motivations for this work was the lack of agreement among those literature spectra. Thus the spectrum of synthetic Fe_3S_4 was measured and used to characterize the sulfur and iron spectroscopy of greigite in MMPs. Some literature spectra of greigite show only a single peak in the L_3 region while others have a two-peak structure with an additional peak at higher energy. Besides possible differences in chemical purity of the Fe_3S_4, the detection mode used to measure the XAS might be another reason for inconsistency among the published Fe $L_{2,3}$ XAS of this mineral (Bauer et al. 2014; Chang et al. 2012a; Letard et al. 2005). Although TEY is a common detection mode to collect XAS, it is a surface-sensitive technique and generally has a probing depth of only a few nanometers. Greigite is relatively easily oxidized when exposed to air and oxidization first occurs at the crystal surface (Santos-Carballal et al. 2016). Thus the XAS collected with TEY mode may be heavily influenced by surface oxidization and surface cleaning. For example, Nolle et al. (2009) reported that a higher oxidation state of Fe was

constituent cell, and that the cells are arranged in a spherical helix, Acosta-Avalos et al. (2012) showed that the net moment is sufficient to align the organism along the magnetic field in the same way as single chains do in unicellular MTB species.

Figure 9, panel A, presents the Fe $L_{2,3}$ spectra of the magnetosomes in the MMP recorded with left and right-circularly polarized X-rays. The inset shows the clusters of magnetosomes from which the Fe $L_{2,3}$ XAS and XMCD spectra were extracted. Compared with the Fe L_3 spectra of abiotic Fe_3S_4 nanoparticles which only shows a single peak at about 708 eV (Figure 2B), the spectrum of biogenic Fe_3S_4 magnetosomes shows an additional feature in the 708.5–710 eV energy range, indicated by the arrow in Figure 9A. Letard et al. (2007) reported a similar feature at a higher energy position than the main L_3 peak in
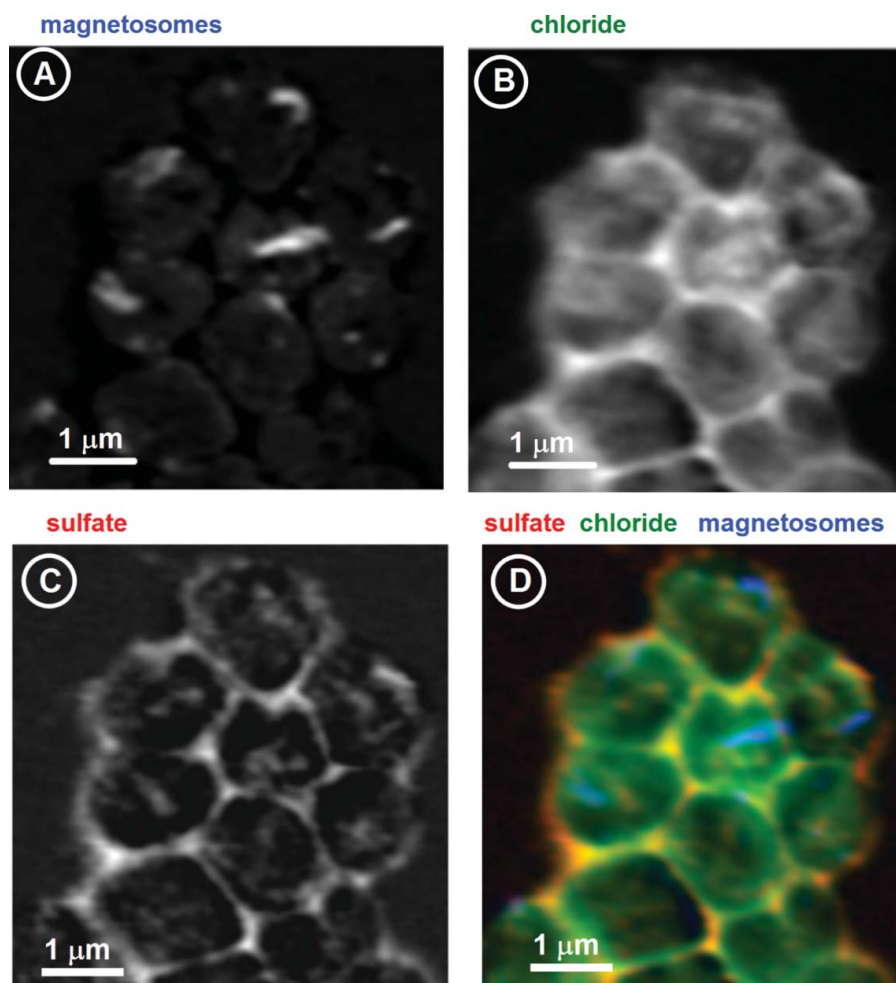
magnetosomes

chloride

sulfate

**sulfate chloride magnetosomes**

Figure 7. Component maps of (A) magnetosomes, (B) chloride, and (C) sulfate regions in a portion of an MMP derived from a 3-component stack-fit analysis of the appended and aligned S 2p/Cl 2p/Fe 2p stack. (D) Re-scaled color composite of the sulfate (red), chloride (green), and magnetosome (blue) maps (Salton Sea).

observed at the surface of crystalline FePt/FeO$_x$ when the detection mode was switched from transmission to TEY. In a recent study, Pattrick et al. (2017) showed that if a freshly synthesized greigite sample was allowed to air oxidize, the Fe L$_3$-edge XAS of Fe$_3$S$_4$ exhibited two distinct peaks, similar to the Fe L$_3$ spectrum of the magnetosomes in MMP (Figure 9). On the other hand, if the freshly synthesized sample was kept strictly anaerobic, the Fe L$_3$-edge XAS of Fe$_3$S$_4$ had only one peak, identical to the spectrum of the synthetic Fe$_3$S$_4$ nanoparticles in this study (Figure 2). Comparison to the results reported by Pattrick et al. (2017) confirms that the Fe$_3$S$_4$ magnetosomes in MMPs were partially oxidized, which is also supported by the time-dependent changes of the XAS of Fe$_3$S$_4$ magnetosomes shown in Figure 10.

The Fe 2p XAS of abiotic Fe$_3$S$_4$ (Figure 2B) shows only one peak in the Fe L$_3$ region. However, Fe$_3$O$_4$, the oxygen counterpart of Fe$_3$S$_4$, always exhibits an additional feature at lower energy, in addition to the main L$_3$ peak (Zhu et al. 2015b). Spender et al. (1972) once reported that Fe$_3$S$_4$ is a semi-metal and proposed two alternative schemes for its electronic structure: one is that it has an average of Fe(II) and Fe(III) on the octahedral sites, similar to that observed in Fe$_3$O$_4$; the other that it has only Fe(II) on octahedral sites. The first scheme was later supported by the results of *ab initio* calculations (Devey et al. 2009).

Bauer et al. (2014) claimed that a large amount of elemental Fe is present in Fe$_3$S$_4$ crystals based on the comparison of his Fe 2p XAS to that of iron. Although the Fe 2p XAS of abiotic Fe$_3$S$_4$ nanoparticles presented in this work has the same shape as those reported by Bauer et al. (2014), the XRD results (Figure 1) are not consistent with the presence of any elemental Fe in the synthesized Fe$_3$S$_4$ nanoparticles. Zhang et al. (2012) calculated the electronic structure of Fe$_3$S$_4$ and reported that Fe$_3$S$_4$ is not half-metallic like Fe$_3$O$_4$ but rather a metal with a complicated Fermi surface. It seems that the electronic structure of Fe$_3$S$_4$ is not understood very well at this time.
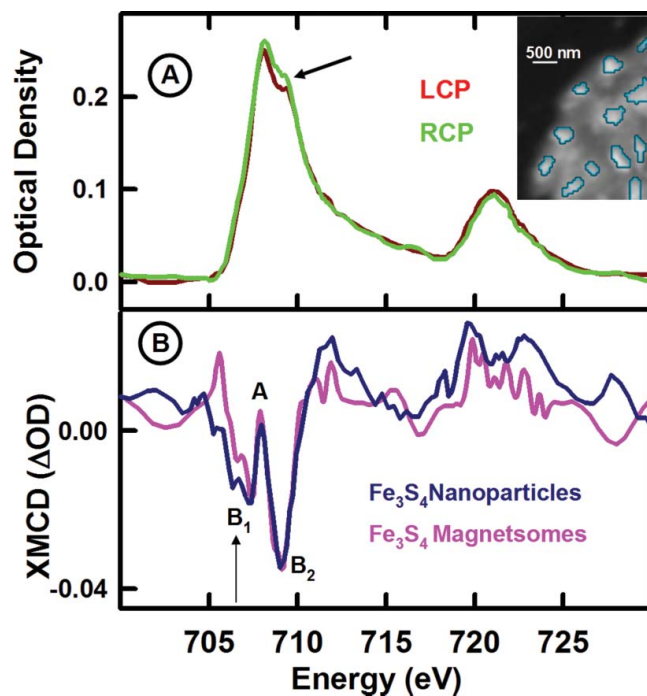
Regarding the magnetic structure of Fe$_3$S$_4$, the XMCD spectra of abiotic and biotic Fe$_3$S$_4$ nanoparticles shown in Figure 9B are significantly different from the XMCD spectrum of Fe$_3$O$_4$ in the L$_3$ region (Goering et al. 2007). It should also be noted that no external magnetic field was applied during the XMCD measurements. The XMCD signals of both the abiotic Fe$_3$S$_4$ nanoparticles and the biotic greigite magnetosomes are considerably weaker than expected from considerations of the bulk magnetic moment of greigite (Chang et al. 2009). For the magnetosomes, this is likely due to cancellation of the magnetic moments from magnetosomes oriented in opposing senses relative to the photon spin vector, since the spectrum reported here is the average over all of the magnetosome chains in the
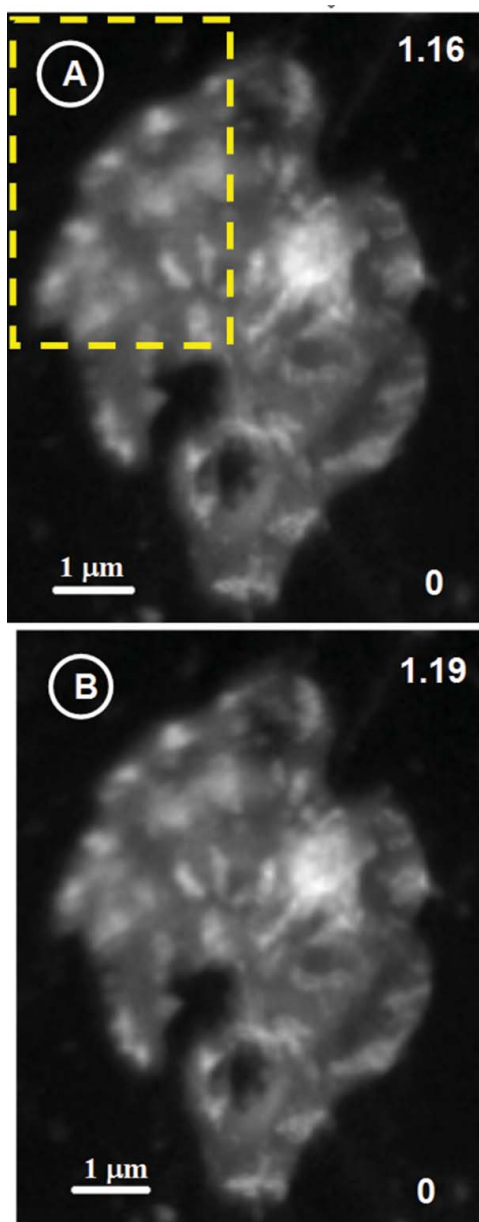
Figure 8. STXM OD images of an MMP recorded at 707 eV with (A) left, and (B) right-circularly polarized X-rays. The yellow dotted rectangle indicates the region where the full XMCD stack was collected (Araruama Lagoon).

Figure 9. (A) Average Fe $L_{2,3}$ spectra of Fe_3S_4 magnetosomes, extracted from the blue outlined regions in the inset image. Spectra recorded with left (LCP, red) and right (RCP, green)-circularly polarized X-rays are plotted on an identical OD scale. The arrow indicates the additional feature observed in Fe_3S_4 magnetosomes but not in Fe_3S_4 nanoparticles (see Fig. 2B). (B) Comparison of the XMCD (LCP–RCP) spectra of abiotic Fe_3S_4 nanoparticles (blue) and the magnetosomes in the MMP (red) (Araruama Lagoon).

while that for Fe_3O_4 is ∼90–92 Am^2/kg (Chang et al. 2008). However, the measured magnetic moment of Fe_3S_4 is only 59 Am^2/kg (Chang et al. 2009). Neutron diffraction indicated that the Fe_3S_4 sample had almost full occupancy of all three Fe sites (Chang et al. 2009), which excluded the possibility that the lower magnetic moment in Fe_3S_4 was due to site vacancy. By comparing the mechanical and electronic properties of Fe_3S_4 and Fe_3O_4 calculated using density function theory, Roldan et al. (2013) reported that Fe_3S_4 is more covalent than Fe_3O_4, which can lead to a lower M_s value of Fe_3S_4. In a recent study,
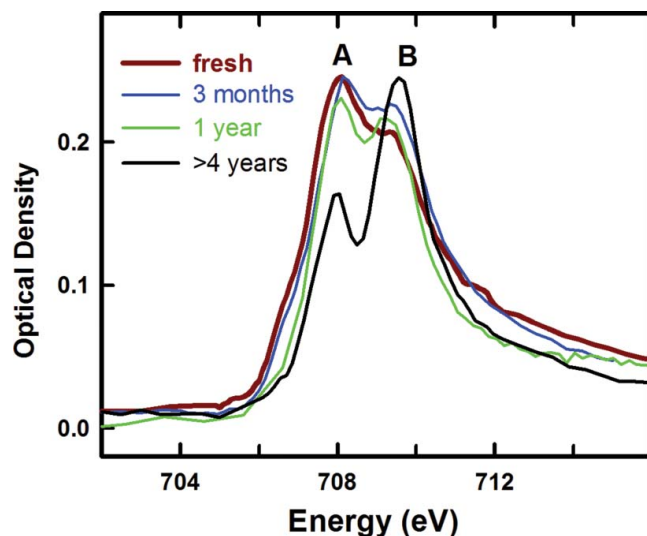
red rectangle area of Figure 8A. A significant fraction of the synthetic greigite sample consists of very small particles, which may be below the super-paramagnetic limit, and thus may have lost the initial magnetic alignment imposed by a strong magnetic field prior to insertion of the sample into the STXM. Further study is needed to fully characterize the strength of the XMCD of greigite.

Multiplet calculations have been used to interpret the XMCD spectrum of Fe_3O_4 (Pattrick et al. 2002). Chang et al. (2012a), using the same computational method, reported that the experimental XMCD spectrum of Fe_3S_4 can only be fit well with O_h Fe^{2+} and O_h Fe^{3+} multiplet signals, but without using a T_d Fe^{3+} multiplet signal. Chang et al. (2012a) attributed the complexity of the XMCD spectrum of Fe_3S_4 to strong covalent iron-sulfur binding in Fe_3S_4, which cannot be reproduced by multiplet calculations. The magnetic saturation (M_s) value for Fe_3S_4 at room temperature is estimated to be about 70 Am^2/kg

Figure 10. Comparison of Fe L_3 XAS of MMP magnetosomes after exposure to air for less than 1 week (fresh), for 3 months, for 1 year, and for over 4 year.

Pattrick et al. (2017) proposed that the magnetic properties of Fe_3S_4 are partially determined by the strong covalency of Fe-S bonding. It has been reported that electron hopping can occur between the high-spin Fe^{3+} and Fe^{2+} ions in the octahedral sites in Fe_3S_4 (Coey et al. 1970; Dekkers, et al. 2000), which results in a high conductivity and high covalency in Fe_3S_4 (Pattrick, et al. 2017). Pattrick et al. (2017) further suggested that such electron hopping between Fe^{2+} and Fe^{3+} can ultimately produce an intermediate oxidization state of Fe, effectively $Fe^{2.5+}$, in the octahedral site of Fe_3S_4, which contrasts with Fe_3O_4, which is thought to have two distinct Fe oxidation states, Fe (II) and Fe (III), in the octahedral sites. The presence of $Fe^{2.5+}$ in the octahedral sites of Fe_3S_4 is believed to produce an overlapping, mainly negative peak in the XMCD spectrum of Fe_3S_4 (Pattrick, et al. 2017), which is labeled B_2 in Figure 2C. Clearly the magnetic structure of Fe_3S_4 is complex. Further experimental and theoretical studies are needed.

Phylogenetically, MMPs are dissimilatory sulfate-reducing bacteria (dSRB) in the *Deltaproteobacteria* class of the *Proteobacteria* phylum (Abreu etal. 2007; Delong et al. 1993; Simmons and Edwards 2007; Wenter et al. 2009; Zhang et al. 2014). Sulfate and sulfide are key components in the sulfur metabolism in dSRB. Sulfate is utilized by dSRB as a terminal electron acceptor and is reduced to sulfide (S^{2-}), which often reacts with many metal ions to form metal sulfides, such as FeS (Jong and Parry 2003). The co-existence of sulfate and sulfide signals in the S 2p spectrum of MMPs suggests that sulfate is involved in the Fe_3S_4 biomineralization process, possibly in sulfur cycling. However, it is also possible that, just as the chloride is of environmental rather than biological origin, much of the observed sulfate is probably a remnant of the high amount of sulfate ions in marine water.

Pósfai et al. (1998a, 1998b) suggested that MMPs do not synthesize greigite directly but initially produce either cubic FeS or mackinawite (tetragonal FeS). In addition, they reported that mackinawite could only be observed in relatively fresh samples because mackinawite crystals convert to greigite in 10 days (Pósfai et al. 1998a, 1998b). In this study, we did not observe any of these proposed Fe_3S_4 precursors. One possible reason might be that any precursors in the cell examined had already transformed to Fe_3S_4 before the STXM measurements.

Summary

In this study, STXM-XAS and STXM-XMCD were used to measure properties of synthetic greigite, and to characterize the chemistry and magnetism of Fe_3S_4 magnetosomes in a multicellular MTB known as MMP. Although the XAS of the synthetic greigite nanoparticles and biotic magnetosome crystals in MMPs are slightly different, the XMCD spectra of the two materials are in good agreement. These results demonstrate that STXM-XMCD is an excellent probe of both the chemical and magnetic properties of MMPs. In addition, as more STXM-XMCD studies are published, this technique promises to be of great value in understanding biomineralization in other organisms.

Acknowledgments

Funding

References

Abreu F, Martins JL, Silveira TS, Keim CN, Lins de Barros HGP, Filho FJG, Lins U. 2007. "*Candidatus* Magnetoglobus multicellularis," a multicellular, magnetotactic prokaryote from a hypersaline environment. Int J Syst Evol Microbiol 57:1318–1322.

Acosta-Avalos D, Dos Santos Azevedo LM, Andrade TS, De Barros HL. 2012. Magnetic configuration model for the multicellular magnetotactic prokaryote *Candidatus* Magnetoglobus multicellularis. Eur Biophys J 41:405–413.

Bauer E, Man KL, Pavlovska A, Locatelli A, Menteş TO, Niño MA, Altman MS. 2014. Fe_3S_4 (greigite) formation by vapor–solid reaction. J Mater Chem A 2:1903–1913.

Bazylinski DA, Frankel RB, Garratt-Reed AJ, Mann S. 1990. Biomineralization of iron sulfides in magnetotactic bacteria from sulfidic environments. In: Frankel RB, Blakemore RP, editors. Iron Biominerals, New York, NY, USA: Plenum Press, p239–255.

Bazylinski DA, Heywood BR, Mann S, Frankel RB. 1993. Fe_3O_4 and Fe_3S_4 in a bacterium.pdf. Nature 366:218.

Bazylinski DA, Frankel RB. 2004. Magnetosome formation in prokaryotes. Nat Rev Microbiol 2:217–230.

Berner RA. 1984. Sedimentary pyrite formation: an update. Geochim Cosmochim Acta 48:605–615.

Chang L, Roberts AP, Tang Y, Rainford BD, Muxworthy AR, Chen Q. 2008, Fundamental magnetic parameters from pure synthetic greigite (Fe_3S_4). J Geophys Res 113:B06104.

Chang L, Rainford BD, Stewart JR, Ritter C, Roberts AP, Tang Y, Chen Q. 2009. Magnetic structure of greigite (Fe_3S_4) probed by neutron powder diffraction and polarized neutron diffraction. J Geophys Res 1:B07101.

Chang L, Pattrick RAD, van der Laan G, Coker VS, Roberts AP. 2012a. Enigmatic X-ray magnetic circular dichroism in greigite (Fe_3S_4). Can Mineral 50:667–674.

Chang L, Winklhofer M, Roberts AP, Dekkers MJ, Horng CS, Hu L, Chen Q. 2012b. Ferromagnetic resonance characterization of greigite (Fe_3S_4), monoclinic pyrrhotite (Fe_7S_8), and non-interacting titanomagnetite ($Fe_{3-x}Ti_xO_4$). GeochemGeophys Geosyst 13:1–19.

Coey JMD, Spender MR, Morrish AH. 1970. The magnetic structure of the spinel, Fe_3S_4. Solid State Commun 8:1605–1608.

Coker VS, Byrne JM, Telling ND, Van Der Laan G, Lloyd JR, Hitchcock AP, Wang J, Pattrick RAD. 2012. Characterisation of the dissimilatory reduction of Fe(III)-oxyhydroxide at the microbe—mineral interface: the application of STXM-XMCD. Geobiology 10:347–354.

Delong EF, Frankel RB, Bazylinski DA. 1993. Multiple evolutionary origins of magnetotaxis in bacteria. Science 259:803–806.

Dekkers MJ, Passier HF, Schoonen MAA. 2000. Magnetic properties of hydrothermally synthesized greigite (Fe_3S_4) II. High- and low-temperature characteristics. Geophys J Int 141:809–819.

Devey EJ. 2009. Computer modelling studies of mackinawite, greigite and cubic FeS, PhD thesis, University College London.

Farina M, Lins de Barros HGP, Esquivel DMS, Danon J. 1980. Ultrastructure of a magnetotactic microorganism. Biol Cell 48:85–88.

Farina M, Esquivel DMS, de Barros HGPL. 1990. Magnetic iron-sulphur crystals from a magnetotactic microorganism. Nature 343: 256–258.

Faivre D, Schüler D. 2008. Magnetotactic bacteria and magnetosomes. Chem Rev 108:4875–4898.

Feng M, Lu Y, Yang Y, Zhang M, Xu Y-J, Gao H-L, Dong L, Xu W-P, Yu S-H. 2013. Bioinspired greigite magnetic nanocrystals: chemical synthesis and biomedicine applications. Sci Rep 3:2994.

Frankel RB. 1984. Magnetic guidance of organisms. Annu Rev Biophys Bioeng 13:85–103.

Goering EJ, Lafkioti M, Gold S, Schuetz G. 2007. Absorption spectroscopy and XMCD at the Verwey transition of Fe_3O_4. J Magn Magn Mater 310:249–251.

Hay SJ, Metson JB, Hyland MM. 2004. Sulfur speciation in aluminum smelting anodes. Ind Eng Chem Res 43:1690–1700.

Heywood BR, Bazylinski DA, Garratt-Reed A, Mann S, Frankel RB. 1990. Controlled biosynthesis of greigite (Fe_3S_4) in magnetotactic bacteria. Naturwissenschaften 77:536–538.

Hitchcock AP, Obst M, Wang J, Lu YS, Tyliszczak T. 2012. Advances in the detection of As in environmental samples using low energy X-ray florescence in a scanning transmission X-ray microscope: arsenic immobilization by a Fe(II)-oxidizing freshwater bacteria. Environ Sci Technol 46:2821–2829.

Hitchcock AP. 2015. Soft X-ray spectromicroscopy and ptychography. J Electron Spectros Relat Phenomena 200:49–63.

Hitchcock AP. 2016. aXis2000 is written in Interactive Data Language (IDL). It is available free for non-commercial use from http://unicorn.mcmaster.ca/aXis2000.html.

Jacobsen C, Wirick S, Flynn GJ, Zimba C. 2000. Soft x-ray spectroscopy from image sequences with sub-100 nm spatial resolution. J Microsc 197:173–184.

Jong T, Parry DL. 2003. Removal of sulfate and heavy metals by sulfate reducing bacteria in short-term bench scale upflow anaerobic packed bed reactor runs. Water Res 37:3379–3389.

Kalirai SS, Bazylinski DA, Hitchcock AP. 2013. Anomalous Magnetic Orientations of Magnetosome Chains in a Magnetotactic Bacterium: Magnetovibrio blakemorei Strain MV-1. PLoS One 8:1–7.

Kalirai SS, Lam KP, Bazylinski DA, Lins U, Hitchcock AP. 2012. Examining the chemistry and magnetism of magnetotactic bacterium Candidatus Magnetovibrio blakemorei strain MV-1 using scanning transmission X-ray microscopy. Chem Geol 300–301:14–23.

Kaznatcheev K V., Karunakaran C, Lanke UD, Urquhart SG, Obst M, Hitchcock AP. 2007. Soft X-ray spectromicroscopy beamline at the CLS: commissioning results. Nucl Instrum Methods Phys Res Sect A Accel Spectrometers Detect Assoc Equip 582:96–99.

Keim CN, Abreu F, Lins U, De Barros HL, Farina M. 2004. Cell organization and ultrastructure of a magnetotactic multicellular organism. J Struct Biol 145:254–262.

Keim CN, Martins JL, de Barros HGPL, Lins U, Farina M. 2006. Structure, behavior, ecology and diversity of multicellular magnetotactic prokaryotes. In: Schüler D, editor, Magnetoreception and Magnetosomes in Bacteria. Berlin, Heidelberg: Springer-Verlag, p103–132.

Kilcoyne ALD, Tylisczak T, Steele WF, Fakra S, Hitchcock P, Franck K, Anderson E, Harteneck B, Rightor EG, Mitchell GE, Hitchcock AP, Yang L, Warwick T, Ade H. 2003. Interferometrically controlled scanning transmission microscopes at the advanced light source. J Synchrotron Radiat 10:125–136.

Koprinarov IN, Hitchcock AP, McCrory C, Childs RF. 2002. Quantitative mapping of structured polymeric systems using singular value decomposition analysis of soft X-ray images. J Phys Chem B 106:5358–5364.

Lam KP, Hitchcock AP, Obst M, Lawrence JR, Swerhone GDW, Leppard GG, Tyliszczak T, Karunakaran C, Wang J, Kaznatcheev K, Bazylinski DA, Lins U. 2010. Characterizing magnetism of individual magnetosomes by X-ray magnetic circular dichroism in a scanning transmission X-ray microscope. Chem Geol 270:110–116.

Lawrence JR, Dynes JJ, Korber DR, Swerhone GDW, Leppard GG, Hitchcock AP. 2012. Monitoring the fate of copper nanoparticles in river biofilms using scanning transmission X-ray microscopy (STXM). Chem Geol 329:18–25.

Lefevre CT, Menguy N, Abreu F, Lins U, Posfai M, Prozorov T, Pignol D, Frankel RB, Bazylinski DA. 2011. A cultured greigite-producing magnetotactic bacterium in a novel group of sulfate-reducing bacteria. Science 334:1720–1723.

Letard I, Sainctavit P, Menguy N, Valet J-P, Isambert A, Dekkers MJ, Gloter A. 2005. Mineralogy of greigite Fe_3S_4. Phys Scr T115:489–491.

Letard I, Sainctavit P, Deudon C. 2007. XMCD at Fe $L_{2,3}$ edges, Fe and S K edges on Fe_7S_8. Phys Chem Miner 34:113–120.

Li D, Bancroft GM, Kasrai M, Fleet ME, Feng X, Tan K. 1995. S K-and L-edge X-ray absorption spectroscopy of metal sulfides and sulfates: applications in mineralogy and geochemistry. Can Miner 33:949–960.

Lin C-R, Tseng Y-T, Ovchinnikov SG, Ivantsov RD, Edelman IS, Fedorov AS, Kuzubov AA, Fedorov DA, Starchikov SS, Lyubutin IS. 2014. Fe_3S_4 and Fe_3O_4 magnetic nanocrystals: magneto-optical and Mössbauer spectroscopy study. Mater Res Express 1:025033.

Lins U, Farina M. 2001. Amorphous mineral phases in magnetotactic multicellular aggregates. Arch Microbiol 176:323–328.

Lins U, Freitas F, Keim CN, De Barros HL, Esquivel DMS, Farina M. 2003. Simple homemade apparatus for harvesting uncultured magnetotactic microorganisms. Brazilian J Microbiol 34:111–116.

Lins U, Keim CN, Evans FF, Farina M, Buseck PR. 2007. Magnetite (Fe_3O_4) and greigite (Fe_3S_4) crystals in multicellular magnetotactic prokaryotes. Geomicrobiol J 24:43–50.

Nolle D, Goering E, Tietze T, Schütz G, Figuerola A, Manna L. 2009. Structural and magnetic deconvolution of $FePt/FeO_x$-nanoparticles using x-ray magnetic circular dichroism. New J Phys 11:033034.

Pattrick RAD, Van Der Laan G, Henderson CMB, Kuiper P, Dudzik E, Vaughan DJ. 2002. Cation site occupancy in spinel ferrites studied by X-ray magnetic circular dichroism: developing a method for mineralogists. Eur J Miner 14:1095–1102.

Pattrick RAD, Coker VS, Akhtar M, Malik MA, Lewis E, Haigh S, O'Brien P, Shafer PA, van der Laan G. 2017. Magnetic spectroscopy of nanoparticulate greigite, Fe_3S_4. Miner Mag 81:857–872. doi:10.1180/minmag.2016.080.114.

Pearce CI, Pattrick RAD, Vaughan DJ. 2006. Electrical and magnetic properties of sulfides. Rev Miner Geochem 61:127–180.

Porreca M, Mattei M, Di Vincenzo G. 2009. Post-deformational growth of late diagenetic greigite in lacustrine sediments from southern Italy. Geophys Res Lett 36:1–6.

Porreca M, Mattei M. 2010. Tectonic and environmental evolution of Quaternary intramontane basins in Southern Apennines (Italy): insights from palaeomagnetic and rock magnetic investigations. Geophys J Int 182:682–698.

Pósfai M, Buseck PR, Bazylinski DA, Frankel RB. 1998a. Iron sulfides from magnetotactic bacteria: structure, composition, and phase transitions. Am Miner 83:1469–1481.

Pósfai M, Buseck PR, Bazylinski DA, Frankel RB. 1998b. Reaction sequence of iron sulfide minerals in bacteria and their use as biomarkers. Science 280:880–883.

Rema T, Lawrence JR, Dynes JJ, Hitchcock AP, Korber DR. 2014. Microscopic and spectroscopic analyses of chlorhexidine tolerance in delftia acidovorans biofilms. Antimicrob Agents Chemother 58:5673–5686.

Rickard D, Luther GW. 2007. Chemistry of iron sulfides. Chem Rev 107:514–562.

Roberts AP. 1995. Magnetic properties of sedimentary greigite (Fe_3S_4). Earth Planet Sci Lett 134:227–236.

Roberts P, Reynolds L, Verosub L, Adam DP, Authigenic A. 1996. Environmental magnetic implications of greigite (Fe_3S_4) formation in a 3 m.y. lake sediment record from Butte Valley, northern California. Geophys Res Lett 23:2859–2862.

Roberts AP, Chang L, Rowan CJ, Horng C-S, Florindo F. 2011. Magnetic properties of sedimentary greigite (Fe_3S_4): an update. Rev Geophys 49, RG1002.

Rodgers F, Blakemore R, Blakemore N, Frankel R, Bazylinski D, Maratea D, Rodgers C. 1990. Intercellular structure in a many-celled magnetotactic prokaryote. Arch Microbiol 154:18–22.

Roldan A, Santos-Carballa D, de Leeuw NH. 2013. A comparative DFT study of the mechanical and electronic properties of greigite Fe_3S_4 and magnetite Fe_3O_4, J Chem Phys 138:204712.

Santos-Carballal D, Roldan A, de Leeuw NH. 2016. Early oxidation processes on the greigite Fe_3S_4 (001) surface by water: a density functional theory study. J Phys Chem C 120:8616–8629.

Simmons SL, Edwards KJ. 2007. Unexpected diversity in populations of the many-celled magnetotactic prokaryote. Environ Microbiol 9:206–215.

Simmons SL, Sievert SM, Frankel RB, Bazylinski DA, Edwards KJ. 2004. Spatiotemporal distribution of marine magnetotactic bacteria in a seasonally stratified coastal salt pond. Appl Environ Microbiol 70:6230–6239.

Snowball IF, Thompson R. 1988. The occurrence of greigite in sediments from Loch Lomond. J Quat Sci 3:121–125.

Spender M R., Coey JMD, Morrish A H. 1972. The magnetic properties and Mossbauer spectra of synthetic samples of Fe_3S_4. Can J Phys 50:2313–2326.

Stöhr J, Siegmann HC. 2006. Magnetism: From Fundamentals to Nanoscale Dynamics. Berlin, Germany: Springer.

Uda M. 1965. On the synthesis of greigite. Am Miner 50:1487–1489.

Wang Y, Lin W, Li J, Pan Y. 2013. High diversity of magnetotactic *Deltaproteobacteria* in a freshwater niche. Appl Environ Microbiol 79:2813–2817.

Warwick T, Andresen N, Comins J, McKean PJ, Shuh DK. 2004. New implementation of an SX700 undulator beamline at the Advanced Light Source. AIP Conf Proc 458–461.

Wenter R, Wanner G, Schüler D, Overmann J. 2009. Ultrastructure, tactic behaviour and potential for sulfate reduction of a novel multicellular magnetotactic prokaryote from North Sea sediments. Environ Microbiol 11:1493–1505.

Zhang ZJ, Chen XY. 2009. Magnetic greigite (Fe_3S_4) nanomaterials: Shape-controlled solvothermal synthesis and their calcination conversion into hematite (α-Fe_2O_3) nanomaterials. J Alloys Compd 488:339–345.

Zhang R, Chen YR, Du HJ, Zhang WY, Pan HM, Xiao T, Wu L-F. 2014. Characterization and phylogenetic identification of a species of spherical multicellular magnetotactic prokaryotes that produces both magnetite and greigite crystals. Res Microbiol 165:481–489.

Zhou K, Zhang WY, Yu-Zhang K, Pan HM, Zhang S Da, Zhang WJ, Yue HD, Li Y, Xiao T, Wu LF. 2012. A novel genus of multicellular magnetotactic prokaryotes from the Yellow Sea. Environ Microbiol 14:405–413.

Zhu X, Hitchcock AP, Bittencourt C, Umek P, Krüger P. 2015a. Individual titanate nanoribbons studied by 3D-resolved polarization dependent X-ray absorption spectra measured with scanning transmission X-ray microscopy. J Phys Chem C 119:24192–24200.

Zhu X, Kalirai SS, Hitchcock AP, Bazylinski DA. 2015b. What is the correct Fe $L_{2,3}$ X-ray absorption spectrum of magnetite? J Electron Spectros Relat Phenomena 199:19–26.

Zhu X, Hitchcock AP, Bazylinski DA, Denes P, Joseph J, Lins U, Marchesini S, Shiu H-W., Tyliszczak T, Shapiro DA. 2016. Measuring spectroscopy and magnetism of extracted and intracellular magnetosomes using soft X-ray ptychography. Proc Natl Acad Sci USA 113, E8219–E8227.